On-ground calibration of the HaloSat science instrument

Anna Zajczyk[a,b,c,d,*], **Philip Kaaret**[a], **Daniel LaRocca**[a], **William Fuelberth**[a], **Hannah C. Gulick**[a], **Keith Jahoda**[c], **Donald L. Kirchner**[a], **Ross McCurdy**[a], **William T. Robison**[a], **Emily Silich**[a]
[a]Department of Physics and Astronomy, University of Iowa, 203 Van Allen Hall, IA 52242, USA
[b]Center for Space Sciences and Technology, University of Maryland, Baltimore County, 1000 Hilltop Circle, MD 21250, USA
[c]NASA Goddard Space Flight Center, Greenbelt, MD 20771, USA
[d]Center for Research and Exploration in Space Science and Technology, NASA/GSFC, Greenbelt, MD 20771, USA

Abstract. HaloSat is a CubeSat-class microsatellite sensitive in the $0.4 - 7.0$ keV energy band and designed to survey the entire sky in search of soft X-ray emission from highly ionized oxygen residing in the halo of the Milky Way galaxy. Those observations will help constrain the mass and spatial distribution of the Milky Way halo and help us understand if hot galactic halos constitute a significant contribution to the overall cosmological baryon budget. In this paper we describe the science instrument calibration products, including channel-to-energy transformation, instrument energy resolution and instrument response, and the on-ground efforts that led to their creation. We also describe the alignment process used to obtain the field of view information for the HaloSat science instrument.

Keywords: X-ray observatories, CubeSats, silicon drift detectors, instrument calibration.

*Anna Zajczyk, anna.zajczyk@nasa.gov

1 Introduction

It has been twenty years since Jordi Puig-Suari and Bob Twiggs[1,2] publicly proposed the CubeSat concept - a class of nanosatellites with standard 1U size (i.e. 10 cm x 10 cm x 10 cm) and maximum mass of 1.33 kg. The CubeSat standard was conceived to help universities train future space scientists and engineers by providing inexpensive access to space for student-built spacecraft, and to provide the community with a low-cost platform for the testing and space qualification of next-generation space technologies. The first CubeSat was launched in 2003 and since then there have been more than 1000 CubeSat-class missions launched. CubeSats are being built by universities, space and defense agencies, private institutions, and amateurs around the world. Today, this standardized platform, in a variety of sizes ranging from the classic 1U up to 12U, is being used not only in its educational capacity and as a test bed for future space technologies, but also for conducting studies of the Earth and near-Earth environment, solar system, and universe.

HaloSat is the first CubeSat-class mission funded by NASA's Astrophysics Division. Its primary scientific goal is to constrain the mass and spatial distribution of hot gas in the Milky Way halo by mapping soft X-ray line emission from highly ionized oxygen. This will help determine how much baryonic matter exists in the hot galactic halo of the Milky Way and if galactic halos are a significant contributor to the overall cosmological baryon budget. The scientific goals are described in more detail in Ref. 3. HaloSat's scientific goals require: X-ray sensitivity in the band that contains emission from highly ionized oxygen ($0.4 - 2.0$ keV), energy resolution sufficient to separate the oxygen emission from other sources ($\Delta E \sim 100$ eV at 600 eV), and a statistical accuracy of better than 10% for oxygen line measurements in directions where oxygen emission is ≥ 5 Line Units (LU or photons s^{-1} cm^{-2} sr^{-1}). This sensitivity can be achieved over the entire sky by an experiment with a grasp (instrument effective area times its field of view) of ~ 20 cm^2 deg^2 and observing efficiency $> 25\%$ in a one year survey. HaloSat meets the grasp goal by using three small commercial silicon drift detectors collimated to ~ 100 deg^2. Table 1 summarizes HaloSat mission goals and requirements, and provides comparison with the achieved instrument performance.

HaloSat is a university-led project with a science team consisting of students (undergraduate and graduate) and early-career scientists whose involvement was crucial in all of the stages of the mission: from instrument design, assembly, and testing, to science operations and data analysis. At the time this is being written the latter two are still ongoing. In this, HaloSat fulfills the main goal of the CubeSat standard, which is to educate and train future space scientists and engineers. Funding for the HaloSat project started in January 2016, and in less than 2.5 years the science instrument was built, tested, integrated with the spacecraft bus, and launched. Nominal science

Table 1 HaloSat mission requirements (R) and goals (G) compared with the achieved instrument performance.

Parameter	Expected performance	Achieved performance
Energy range (R)	$0.4 - 2.0$ keV	$0.4 - 7.0$ keV
Energy resolution (R)	~ 100 eV at 600 eV	84.9 ± 2.7 eV at 676.8 keV
	–	91.1 ± 1.4 eV at 1742.5 keV
Effective area[†]	–	6.38 mm^2 at 676.8 keV
	–	11.29 mm^2 at 1742.5 keV
Field of View[††]	–	115.02 ± 0.24 deg^2
Grasp[*] at ~ 600 eV (G)	~ 20 cm^2 deg^2	~ 17.7 cm^2 deg^2
Number of functioning detectors	–	3
SDD operating temperature	–	−30°C

[†] The effective area is given for a single detector unit.
[††] The field of view value is a response-weighted effective field of view averaged over three detector units.
[*] The instrument grasp is calculated assuming all three detectors are functional, i.e. grasp $= 3\times$ effective area $\times$ field of view. The grasp goal results from the statistical accuracy requirement for oxygen line measurements (i.e. 10% or better for a direction with oxygen emission at the level of ≥ 5 LU) and the predicted observing efficiency ($> 25\%$) in a one year survey. To achieve the required statistical accuracy, an instrument with a smaller grasp will effectively need to increase the observing time.

operations started in October 2018 and are expected to continue until re-entry into the atmosphere in December 2020.

This paper describes the ground calibration of the HaloSat science instrument. An overview of the instrument design is presented in Sec. 2. The experimental setup is described in Sec. 3.1. Results on instrument gain, energy resolution and noise are presented in Sec. 3.2 and 3.3. Section 3.4 discusses the instrument spectral response and effective area. Finally, the instrument field of view measurements are described in Sec. 4, and conclusions are presented in Sec. 5.

2 Science instrument overview

The HaloSat satellite has a 6U form factor with spacecraft bus dimensions of 10.5 cm × 22.5 cm × 36.5 cm and a total mass of 12 kg.[4] A 2U volume is allocated for spacecraft avionics and payload-to-spacecraft interface, and 4U is allocated to the science instrument. The spacecraft bus and avionics were built by Blue Canyon Technologies, while the science instrument was designed, built and tested at the University of Iowa. Figure 1 shows the science instrument during assembly (left panel) and the fully assembled science instrument during its integration with the spacecraft (right panel).

The science instrument is enclosed in an aluminum chassis with dimensions of 8.7 cm × 22.0 cm × 17.0 cm. The chassis is divided into three identical compartments with each compartment carrying a single detector unit. Each detector unit consists of a silicon drift detector (SDD) mounted on an aluminum baseplate with a copper-tungsten passive shield that surrounds the SDD on five sides. The sixth side has a circular opening that provides an unobstructed path for the incident X-rays. Front-end signal processing electronics are mounted on the underside of the baseplate. A high-voltage power supply is mounted in front of the detector baseplate, while analog and digital processing unit (DPU) boards close off the top of the detector compartment. The left panel of Fig. 1 shows the relative placement of the detector unit components inside the chassis compartment. The fully assembled instrument integrated with the spacecraft bus is shown in the right panel of Fig. 1. Detector units are referred to using numbers encoded in their DPUs which are 14, 54 and 38 as viewed from left to right in Fig. 1. A detailed description of the HaloSat science-instrument mechanical and electrical design can be found in Ref. 5. Each detector unit can be operated independently of the others - a solution that was implemented in the instrument design in order to avoid single point failures and to allow for operation of only one or two detector units at a time depending on the power constraints.

It is important to note that a substantial effort went into minimizing the adverse impact of any potential electromagnetic interference between individual detector units, and between the science instrument and the components of the spacecraft bus, on the performance of the detector units. Design of the flight chassis and the detector electronics (described above) allowed to enclose each detector unit in its own Faraday cage. Connecting the ground plane of the analog board to the chassis ground with a resistor allowed to minimize the noise pickup. After integrating the science instrument with the spacecraft bus, a series of tests was carried out to determine any potential source of electromagnetic interference between the bus subsystems (radio, reaction wheels, etc.) and the detector units. In all of the performed tests, the properties of the noise component below ~ 300 eV (its magnitude and width) in the spectra of individual detector units were used to monitor and assess the magnitude of the electromagnetic interference. The tests showed no measurable interference between the detector units and from any of the spacecraft subsystems. Minimizing the effects of the electromagnetic interference was crucial to achieving the required instrument performance around 600 eV (see Sec. 1).

The HaloSat science instrument uses silicon drift detectors manufactured by Amptek, Inc.[6] to detect X-rays. The SDD's radiation-sensing element (Si chip) has an active area of 17 mm^2 and is encapsulated in a TO-8 package alongside its multilayer collimator (MLC) and two-stage thermoelectric cooler. During operations the Si chip is cooled down to $-30°$C, but the entrance window is always at ambient temperature, which should help prevent the buildup of the contaminants on the window. The entrance window is a C-Series C1 window made of 150 nm thick silicon nitride layer coated with 250 nm of aluminum. Amptek also offers its SDD detectors with a C-Series C2 entrance window. Similarly to the C1 type, the C2 window is made of silicon nitride covered with a layer of aluminum. However, the overall thickness of the C2 window is smaller (40 nm of silicon nitride and 30 nm of aluminum) resulting in better transmission around 600 eV (it is $\sim 62\%$ and $\sim 29\%$ for the C2 and C1 type, respectively). The advantage of the C1 window over the C2 type is

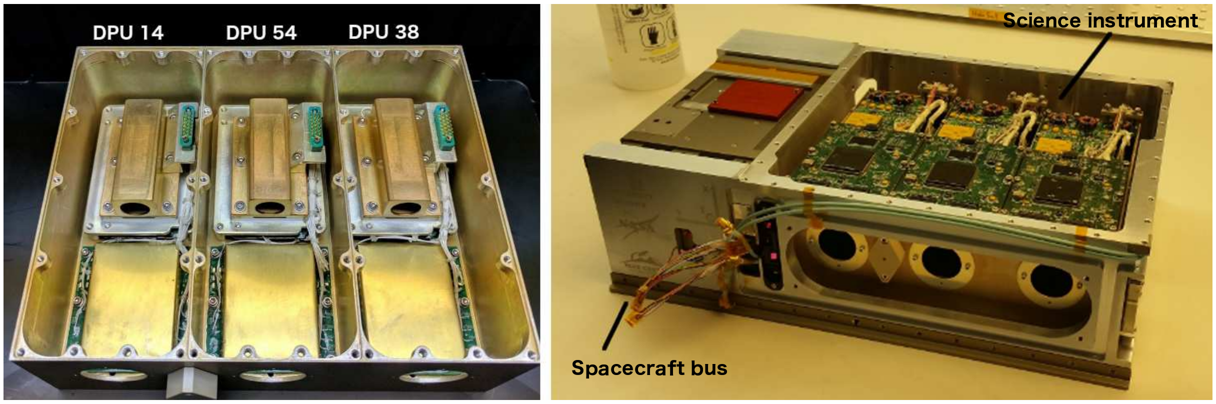

Fig 1 Left: Science instrument during assembly. The instrument chassis is subdivided into three separate compartments, each of which harbors a detector unit with its signal processing electronics. Right: Science instrument (fully assembled) integrated with the spacecraft bus.

its opaqueness to the radiation in the visible and infrared. The HaloSat detectors will be exposed to visible/IR photons during flight. Therefore, minimizing adverse effects of such exposure is an important step to improve detector performance. Considering these factors, the C1 windows were chosen for the HaloSat X-ray detectors.

3 Instrument performance characterization

In order to provide high-quality science data, the science instrument needs to undergo a variety of on-ground tests that mimic flight conditions in order to understand and characterize its performance under those conditions. These tests measure the detector energy calibration, energy resolution, and noise behavior, which are combined to produce the detector response function.

The HaloSat detector units were calibrated individually and at a representative range of temperatures (between $-25°$C and $45°$C). It was observed that the detectors' gain show dependence on the temperature. However, with the exception of the gain behavior, the differences between the performance of the detector units were not significant for the statistical precision achieved in the HaloSat calibration data. For that reason, the gain information was separated from the response

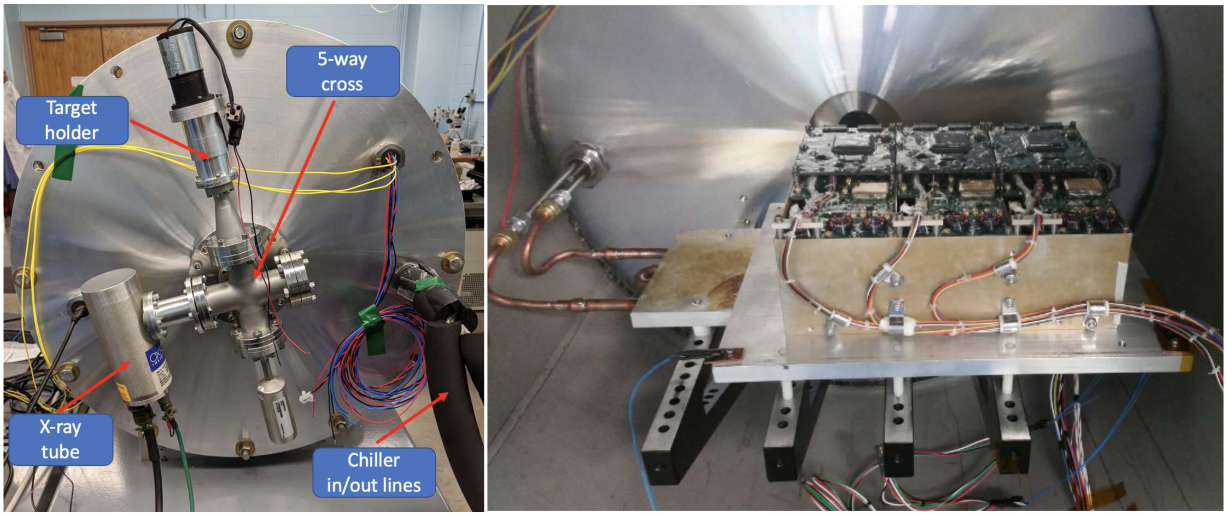

Fig 2 Experimental setup during thermal-vacuum tests. Left: Backside of the TVAC chamber with five-way cross. The target material, mounted on the target holder, is positioned in the center of the cross. Right: The science instrument mounted inside the TVAC chamber. The amber-brown substance visible on the top surface of the thermal plate is the thermal-vacuum grease. Copper lines circulating fluid between the thermal plate and the chiller are visible on the left. One of the chamber temperature sensors is clearly visible on the bottom left corner of the mounting plate.

generation process allowing for the creation of an average response suitable for all three DPUs. The following sections (Sec. 3.1 through Sec. 3.4) describe in-detail the calibration tests and the analysis that led to creation of the single response function and to the determination of the individual detector gains. The interested reader is referred to Ref. 3, where the on-orbit check of the HaloSat spectral response and effective area is discussed.

3.1 Experimental setup for thermal-vacuum tests

In order to mimic flight conditions, a thermal-vacuum (TVAC) test setup (Fig. 2) was built at the University of Iowa. It consisted of a vacuum chamber capable of maintaining a 100 mTorr vacuum under continuous pumping. A thermal plate was mounted inside the chamber, and its temperature was regulated by circulating fluid through copper tubing embedded in the plate. The fluid was heated or cooled by an external chiller. The science instrument was bolted to a mounting plate, which was then bolted to the thermal plate. Thermal-vacuum grease was applied between the thermal plate and the mounting plate. The Apiezon H vacuum grease was used because of its good thermal conduction and low outgassing properties. The latter characteristics was important to prevent the detector windows from contamination. Temperature sensors were bolted to the mounting plate at each corner of the plate. An additional temperature sensor was mounted on the outside of the vacuum chamber. Temperature was recorded every 2 seconds.

Each detector unit is equipped with four temperature sensors: one on the detector baseplate, two on the analog board, and one on the DPU board. There is also a temperature sensor inside the SDD's TO-8 package that monitors the temperature of the silicon X-ray sensing element. During operation, the Si chip temperature is kept at -30°C. The cool down process is initiated immediately after the detector is powered on and is governed by a proportional-integral-derivative (PID) controller implemented into the detector operating system.[5] It takes about 60 seconds for the controller to cool down the Si chip from 20°C to -30°C with a minimal overshoot during the initial cool-down phase. During nominal operations the PID controller keeps the Si chip temperature to within ± 0.5°C of the -30°C setpoint. The initial cool-down phase is clearly visible in Fig. 3 in the plot of the Si chip temperatures (blue points) as the large excursions from the setpoint (dot-dashed line) at the initial phase of each data cluster. The large excursions from the setpoint visible at the end phase of each data cluster are the result of the Si chip warming up after the PID control is switched off prior to the full system shutdown. The Si chip temperature is further referred to as the SDD temperature. Temperatures from the five sensors in the detector unit are recorded as a part of housekeeping data every 8 seconds.

During the TVAC tests, when the system was close to reaching thermal equilibrium (i.e. after ~ 45 min from when the cooling/heating started) the temperature gradient across the mounting plate was $\lesssim 1$°C for the chiller setpoints above 0°C, and $\lesssim 2$°C for the chiller setpoints below 0°C.

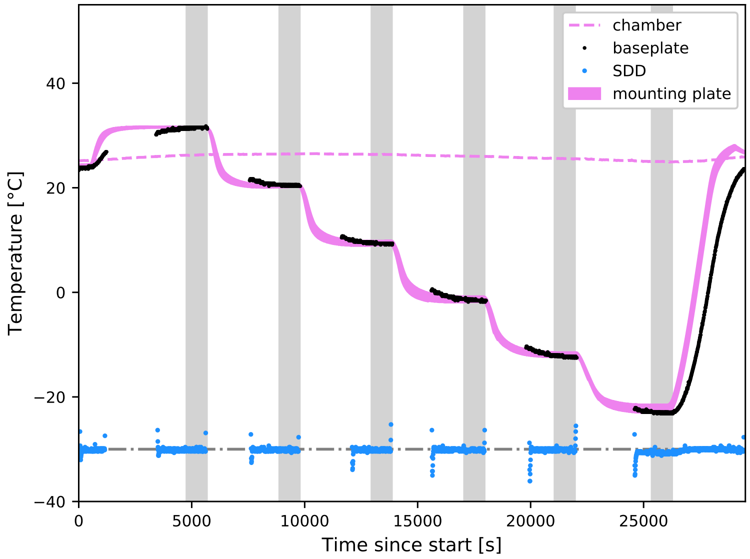

Fig 3 Temperature profile for the DPU 38 TVAC test. Shown are readouts of the baseplate temperature sensor (black points), the SDD temperature sensor (blue points), and the sensor mounted on the outside of the TVAC chamber (violet dashed line). The violet band shows the temperature of the mounting plate. Gray vertical bands show good time intervals identified for this test. The dot-dashed gray line shows a temperature of $-30°$C.

The width of the violet band in Fig. 3 represents the temperature gradient across the mounting plate. During the cool-down or warm-up phase the band gets wider, but when the system gets closer to the thermal equilibrium the width of the band decreases. The difference between the temperature of the mounting plate (given as an average of its four sensors) and the temperature of the baseplate is within $1.5°$C for the temperature range probed in the TVAC tests. In the data analysis that follows, the temperature read by the sensor mounted on the detector baseplate was used as an indicator of the detector unit temperature during the TVAC tests.

In order to monitor instrument response to changing thermal conditions, the TVAC chamber was equipped with an X-ray scattering source consisting of a shielded X-ray tube (Oxford Instruments Jupiter 5000 series with Mo anode) and a scattering target mounted in the center of a five-way cross (see the left panel of Fig. 2). There was no direct line of sight between the Jupiter

X-ray tube and the instrument, and only X-rays scattered off of the target or chamber walls could reach the detector, thus, minimizing the continuum level in the observed spectra. The entrance aperture through which the X-ray beam from the scattering source enters the TVAC chamber is visible in the right panel of Fig. 2 as a circular opening on the back wall of the chamber. A teflon (PTFE) target produced a fluorescence emission line from Fluorine (F Kα line) at 676.8 eV. The X-ray beam also illuminated the stainless steel walls of the five-way cross and the aluminum target holder leading to fluorescence lines from aluminum, chromium and iron. The characteristic emission from those elements is spread across the HaloSat energy band.

Due to the source configuration, only one detector unit was illuminated at a time and each TVAC profile was performed three times in order to complete the calibration of the science instrument. ^{55}Fe radioactive sources were placed in front of the field of view aperture of the two units not illuminated with the scattering source so the health of each unit could be monitored throughout the TVAC tests.

Thermal simulations of the spacecraft in its low-Earth orbit were used to determine lower and upper temperature bounds for the TVAC tests. The simulations predicted that the instrument will be subject to temperatures between -20°C and 24°C. The external chiller was programmed to vary the thermal plate temperature between -25°C and 45°C, which includes the temperature range predicted by the thermal simulations. Figure 3 shows an example of a temperature profile used during one of the HaloSat TVAC tests and the temperature response of a detector unit to this test. The test temperature profile consists of a number of temperature setpoints where the system is left to dwell for about an hour, during which time the X-ray data were collected for all three units. The dwell time of ~ 1 hr was selected so that the system elements near the SDD detector had enough time to equilibrate close to the temperature setpoint and provide at least 600 seconds

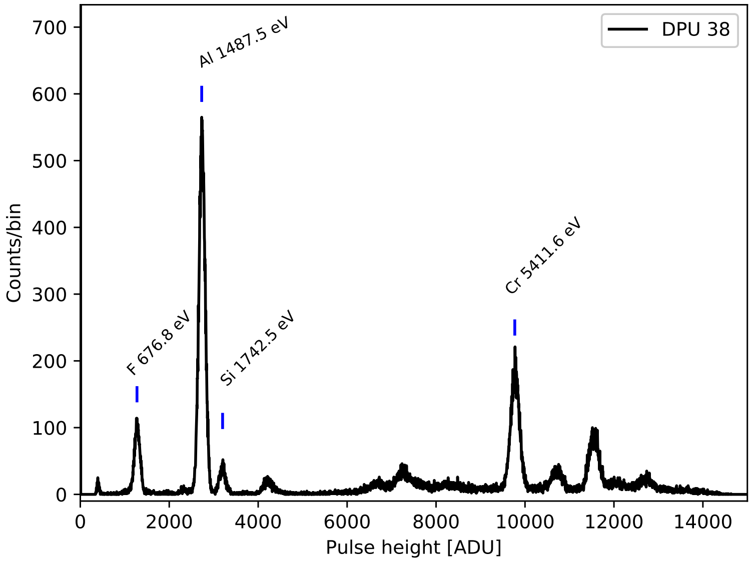

Fig 4 Example of a calibration spectrum obtained during TVAC tests. The plot shows data for DPU 38.

of data during which the baseplate temperature remained constant to within $\pm 0.5°$C. An example of time intervals meeting those criteria is depicted in Fig. 3 with gray vertical bands. For each identified time interval an X-ray spectrum was created and analyzed.

3.2 Energy calibration

Figure 4 shows an example of a calibration spectrum obtained with the DPU 38 detector unit illuminated with the X-ray scattering source during the TVAC tests. A number of emission lines from elements like fluorine, aluminum, silicon and chromium can be clearly identified. The strongest line is a blend of aluminum Kα_1, Kα_2 and Kβ_1 characteristic lines. The line to the left of the Al peak is a fluorine Kα_1 line, while the line to the right of the Al peak is a blend of silicon K-shell lines. The line at around 9800 Analog-Digital Units (ADU) is a blend of chromium Kα_1 and Kα_2 characteristic lines. Lines visible above 10000 ADU are blends of various K-shell lines from chromium, nickel, manganese and iron. The fluorine line is a fluorescence line from the PTFE

Table 2 List of emission lines and their characteristic energies.

Line type	Energy† (eV)
F Kα_1	676.8
Al Kα_1+Kα_2+Kβ_1	1487.5
Si Kα_1+Kα_2+Kβ_1	1742.5
Cr Kα_1+Kα_2	5411.6

† Adopted energies are weighted averages with intensities and energies from Ref. 7.

target. The aluminum line is dominated by the fluorescence from the target holder, while Cr, Mn, Ni and Fe are fluorescence lines from the stainless steel walls of the five-way cross. The Si line originates from the detector C1 window material. Four emission lines were used in the energy calibration of the science instrument: F Kα_1, Al K-shell blend, Si K-shell blend and Cr Kα blend. Table 2 lists the energies of the four selected emission lines.

The energy calibration is approximated with a linear function $E = c_1\, PH + c_2$, where the pulse height PH is in ADU and the photon energy E is in eV. Good quality data were extracted from the full data set using the baseplate temperature stability criterion (see Sec. 3.1). This yielded data runs with exposure times $\gtrsim$ 600 seconds. There were 29, 35 and 15 individual data runs for DPUs 14, 54 and 38, respectively. The number of calibration runs for DPU 38 is smaller than for the other two detector units because the analog board of that unit experienced failure after the primary TVAC calibration campaign and had to be replaced with a flight spare. The TVAC calibration of DPU 38 had to be repeated while the original data set for that unit was discarded.

For each spectrum, the four emission lines (Tab. 2) were fit with a model that was a sum of a Gaussian and a constant. The constant represents a small, but non-negligible continuum present in the spectra. The resulting emission line centroids were then fit to the energy calibration transformation. The energy calibration coefficients (c_1, c_2) were determined for a number of temperatures

Table 3 Temperature-dependent energy calibration coefficients for the HaloSat detector units. The temperature dependence of the coefficients can be approximated with a parabola $c_1 = a_1 T^2 + a_2 T + a_3$ and a linear function $c_2 = a_1 T + a_2$, where T is the baseplate temperature. The a_i values and their errors are given in the third and fourth column.

Coefficients		a_i	a_i
c_i	a_i	value	error
DPU 14			
c_1	a_1	0.00000186	0.00000027
	a_2	0.00000584	0.00001060
	a_3	0.54375	0.00012
c_2	a_1	-0.14	0.01
	a_2	-29.98	0.29
DPU 54			
c_1	a_1	0.00000066	0.00000024
	a_2	-0.00001471	0.00001079
	a_3	0.54937	0.00014
c_2	a_1	-0.181	0.013
	a_2	-35.51	0.40
DPU 38			
c_1	a_1	0.00000234	0.00000014
	a_2	-0.00004721	0.00000275
	a_3	0.55647	0.00007
c_2	a_1	-0.14	0.01
	a_2	-32.93	0.22

spread over the $-25°$C to $45°$C operational range.

While the temperature of the X-ray sensing element in each of the SDDs is actively controlled and kept at $-30°$C during instrument operation (see Sec. 3.1), the printed circuit board carrying the front-end electronics for signal shaping and amplification (mounted under each of the detector baseplates) is subject to changing thermal conditions. This may result in the detector performance depending on temperature. The TVAC tests show that the energy calibration coefficients exhibit a slight dependence on the system temperature. The temperature dependence of the c_1 and c_2 coeffi-

Table 4 Energy calibration coefficients, c_1 and c_2, calculated for the median in-flight temperature T_{median}.

DPU Unit	T_{median} (°C)	Coefficients c_1	c_2
14	5.6	0.544	-30.783
54	5.8	0.549	-36.556
38	6.4	0.556	-33.789

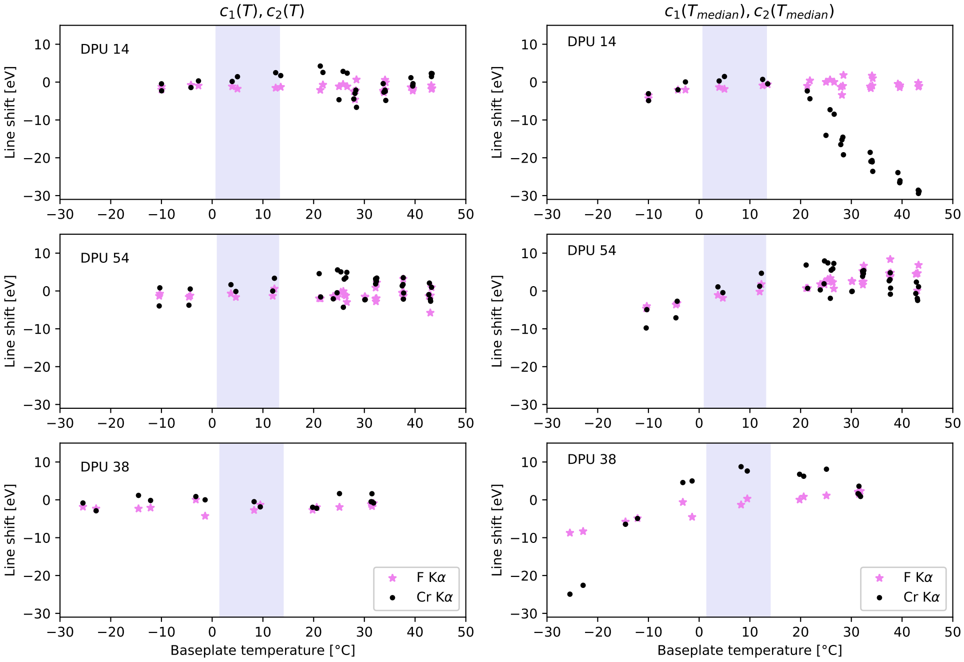

Fig 5 Line shifts as a function of the instrument temperature for F Kα (violet stars) and Cr Kα (black dots). The left column shows the case where the temperature-dependent energy calibration was used (see Tab. 3). The right column uses the pulse height to energy relation for the median in-flight temperature (see Tab. 4). The shaded regions represent the temperature range which includes 90% of the HaloSat observations collected during the first six months of operation. The results for DPUs 14, 54 and 38 are shown in the top, middle and bottom row, respectively.

cients can be approximated with a parabola and a linear function, respectively. The parameters of those two functions obtained for each detector unit are presented in Tab. 3.

The line shifts (defined as a difference between the emission line centroid measured in the energy calibrated spectrum and the line's characteristic energy as given in Tab. 2) were used to study the accuracy of the temperature-dependent energy transformation. Due to the limited size of our TVAC data set, the same spectra used to determine the energy calibration, were used to study its accuracy. The line shifts for the F Kα and the Cr Kα emission lines, which lie at the opposite ends of the HaloSat energy band, are presented in the left column of Fig. 5. The line shifts at both energies show consistent behavior across the full temperature range. We use the largest absolute line shift to represent the accuracy of the energy calibration. At the lower end of the HaloSat energy band, the accuracy is 5 eV, 6 eV and 4 eV for DPUs 14, 54 and 38, respectively. While at the upper end, it is 7 eV, 6 eV and 3 eV for DPUs 14, 54 and 38, respectively. The accuracy is small compared to the HaloSat energy resolution (Sec. 3.3) and comparable to the statistical precision with which narrow lines are fit in the HaloSat data.[3]

We also investigated if a simpler approach to the energy calibration can provide similar results to the temperature-dependent one. The simpler approach would be to eliminate the temperature dependence of the c_1 and c_2 coefficients, and to only have to ever use a single (c_1, c_2) set. The first six months of the HaloSat on-orbit data, collected between September 2018 and February 2019, were used to determine the range of the temperatures to which the instrument was exposed during that time. The shaded regions presented in Fig. 5 show the on-orbit temperature range that includes 90% of the data. The temperatures seen in flight lie well within the temperature range probed in the TVAC tests. For each detector unit, the median of the on-orbit temperatures T_{median} was used to calculate the (c_1, c_2). Table 4 shows the calculated values. The line shifts obtained with the T_{median} energy calibration coefficients are presented in the right column of Fig. 5 and show much larger residuals, particularly towards the extremes of the allowed temperature range. HaloSat standard products are produced with the temperature-dependent coefficients.

Table 5 Temperature-averaged energy resolution (FWHM) measured at four energies for each flight detector.

DPU unit	FWHM (eV) F Kα	 Al K-shell	 Si K-shell	 Cr Kα
14	88.3 ± 2.9	94.5 ± 1.9	92.8 ± 4.6	133.4 ± 2.0
38	81.8 ± 1.5	89.6 ± 1.5	89.6 ± 4.8	130.0 ± 1.8
54	84.7 ± 3.1	92.7 ± 1.8	90.9 ± 6.0	133.4 ± 1.9

3.3 Energy resolution and electronic noise

The TVAC data also characterize the energy resolution as a function of photon energy and instrument temperature. The full width at half maximum (FWHM) of the Gaussian fit to the emission line was measured for the four calibration lines listed in Tab. 2. Figure 6 shows the fit FWHM as a function of instrument temperature for DPU 38. Although there is a slight linear dependence of the FWHM on temperature (degradation of FWHM with increasing temperature) for the Al 1487.5 eV line, for all of the emission lines the variation in the FWHM across the $-25°\mathrm{C}$ to $45°\mathrm{C}$ temperature range is small enough to be approximated with a constant. The dot-dashed lines in Fig. 6 represent the temperature-averaged FWHM values. Values for all DPUs are reported in Tab. 5.

In the simplest case, the energy resolution of a semiconductor detector depends on a statistical noise arising from the discrete nature of the measured signal and a noise arising in the detector signal processing electronics.[8,9] The total energy resolution, FWHM_{total}, is then the quadrature sum of the individual sources of fluctuations:

$$\mathrm{FWHM}_{total} = \sqrt{\mathrm{FWHM}^2_{noise} + 8ln(2)\epsilon F E}\,, \tag{1}$$

where FWHM_{noise} represents the electronic noise, while the second component represents the statistical nature of the signal. Here ϵ is the average energy required to create an electron-hole pair,

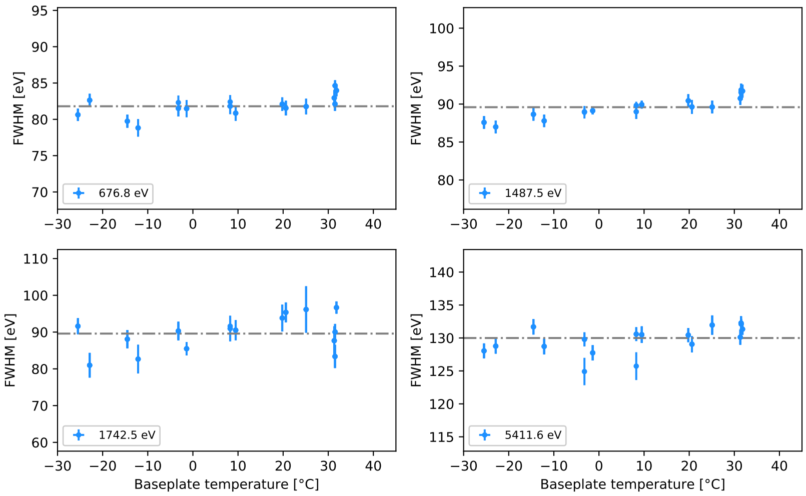

Fig 6 Energy resolution as a function of the instrument temperature. Energy resolution was measured for four calibration lines: F Kα (top left), Al K-shell (top right), Si K-shell (bottom left) and Cr Kα (bottom right). Blue points show measurements, while dot-dashed lines represent the temperature-averaged FWHM values (see Tab. 5). The plots show data for DPU 38. The other two detector units show similar behavior.

F is the Fano factor, and E is the photon energy. For silicon drift detectors, $\epsilon \simeq 3.66$ eV and $F \simeq 0.114$.[8–10] Equation 1 then can be used to determine the magnitude of the electronic noise component. Figure 7 shows the electronic noise value as a function of instrument temperature for all three detector units. We conclude that the electronic noise component in the HaloSat detector units is approximately constant with a temperature-averaged value of 78.5 ± 2.4 eV for DPU 14, 75.0 ± 2.5 eV for DPU 54 and 70.4 ± 1.9 eV for DPU 38.

3.4 Response of the silicon drift detectors

There are three components that need to be taken into account in order to properly model the response of a silicon detector: generation of a main photopeak, generation of escape peaks, and effects arising from charge loss. The main peak arises from events for which the entire liberated charge is collected from the detector active volume. Its shape can be approximated with a Gaussian, which arises from statistical fluctuations in the amount of charge that is liberated in photon

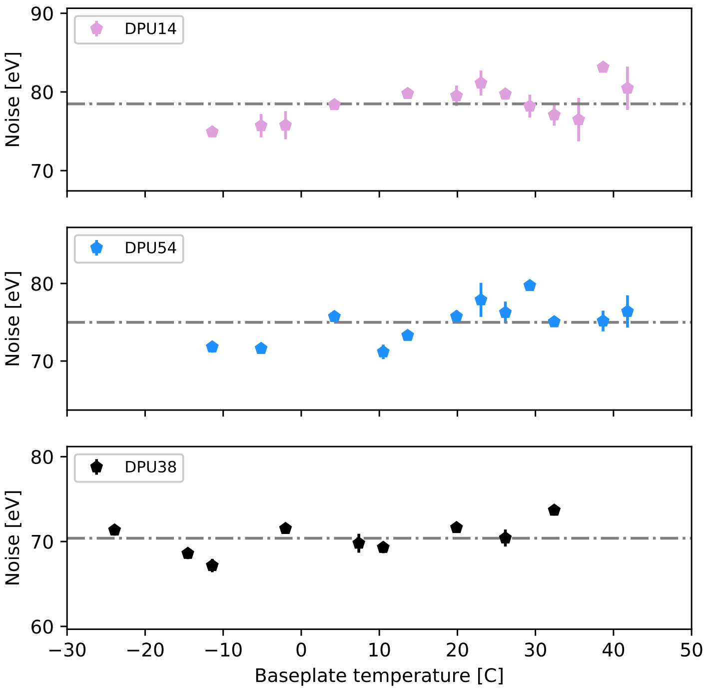

Fig 7 Electronic noise, FWHM_{noise}, as a function of the instrument temperature. Data for DPUs 14, 54 and 38 are shown in the top, middle and bottom panel, respectively. For most data points the error bars are comparable with the symbol size used. The dot-dashed lines represent the temperature-averaged values of the electronic noise.

interaction. Eq. 1 describes the width of the main peak. An escape peak is formed when the characteristic X-rays from silicon escape the detector volume following the primary photoelectric absorption. Escape peaks occur in the spectrum below the main photopeak at an energy equal to the full energy of the main peak minus the respective Kα or Kβ characteristic energy of silicon. The two important structures that arise in the spectra of silicon detectors that are related to the charge loss phenomena are: a tail that extends from the main peak towards low energies, and a shelf that extends from zero to the full photon energy. Detailed description of these effects can be found in Ref. 10 and references therein.

To model the response of HaloSat's SDDs, we have used Scholze & Prokop code[10] that was kindly provided to us by Dr. Jack Steiner of the Neutron star Interior Composition Explorer (NICER) instrument team.[11] The silicon drift detectors used by HaloSat are identical to the ones used by NICER except for the type of the entrance window and the dimensions of the internal collimator.[12] The differences affect the energy dependent effective area and the grasp but not the response function.

To model the response of the HaloSat instrument, we adjusted the relevant detector parameters using the ground calibration data (see Sec. 3.2 and 3.3) and the manufacturer's information on the Amptek C1 window. We used TVAC ^{55}Fe spectra to check the simulated response function and fine-tune its tail and shelf parameters. Because the HaloSat detectors show similar spectral performance, we use a single response model to simulate behavior of all three detectors, and adopt an average electronic noise component of 74.6 eV. The left panel in Fig. 8 shows good agreement between the ^{55}Fe calibration spectrum and the modeled response. We did not fine-tune the shape of the noise peak below 400 eV, which sets the lower limit of the HaloSat energy band. The upper limit of 7 keV is set by the signal processing electronics, which become non-linear above this point.

Effective area (EA) calculations for the HaloSat detectors included the following effects: i) transmission through the C1 window, ii) transmission through the MLC, iii) transmission through the SDD's dead layer, and iv) absorption in the SDD's active volume. We evaluated the model with manufacturer information provided to us by Amptek, Inc.. The Si chip is 500 μm thick with a 0.1 μm thick dead layer. In the HaloSat energy range, the MLC is opaque to X-rays, thus, limiting the geometrical area of the detector to 17 mm^2. The MLC shields the edges of the Si chip where charge collection is known to be inefficient. Tabulated transmission values for the C1 window, calculated using nominal window thickness, were supplied by HS Foils, Oy. The right panel of

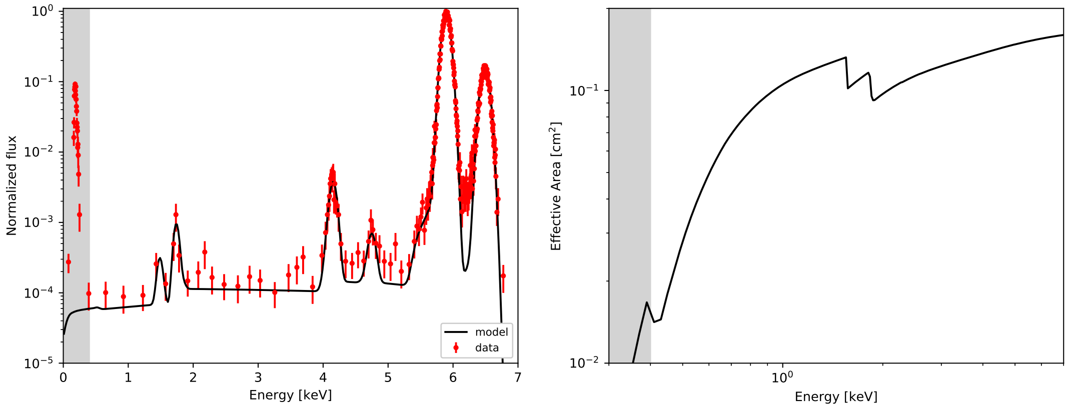

Fig 8 Left: Comparison of a simulated response function (solid black) with one of the ^{55}Fe calibration spectra obtained with DPU 14 detector unit (red points). Right: Effective area calculated for a single HaloSat detector. The shaded gray area (energies below 400 eV) is not modeled in the response calculations.

Fig. 8 shows the effective area calculated for a single HaloSat detector. The effective area in the HaloSat science band (where emission from highly ionized oxygen is expected) is 4.301 mm^2 and 5.979 mm^2 at 561 eV and 653 eV, respectively. We use the same effective area for all three detector units. The effective area calculations were verified in orbit with observations of the Crab Nebula.[3]

The HaloSat response files are compatible with the XSpec spectral fitting software[13] and available from the High Energy Astrophysics Science Archive Research Center (HEASARC).[14]

4 Field of view of the science instrument

The field of view (FoV) of each HaloSat detector unit is constrained by an aluminum washer placed over the opening at the front wall of the detector compartment. The washers are not yet installed in the left panel of Fig. 1, but are present in the right panel of Fig. 1. The use of the FoV washers allows ground adjustment of the detector co-alignment without the need for modifying the chassis itself.

Alignment and field of view were measured by scanning a collimated X-ray source horizontally

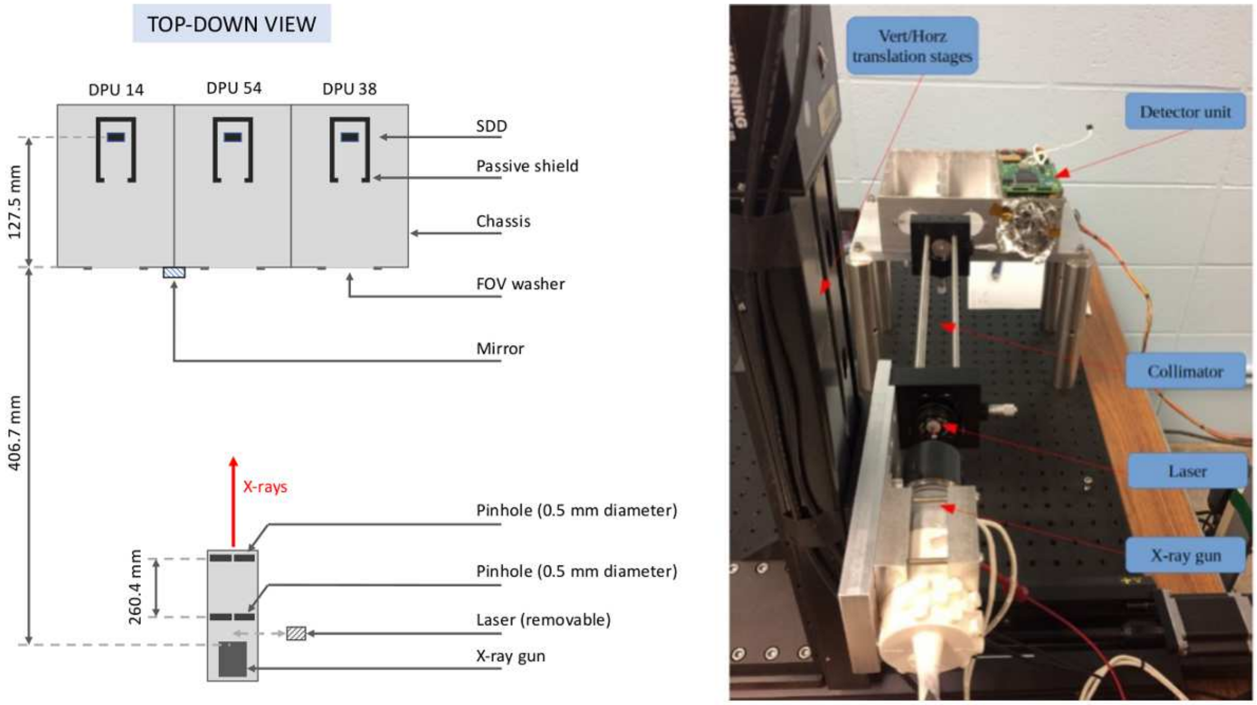

Fig 9 Alignment setup built at the University of Iowa to measure the field of view and the pointing of the HaloSat detector units. Left: Schematic drawing showing a top-down view of the alignment system (not to scale). The distance between the X-ray gun and the closest of the pinholes is 82.8 mm. Right: Photo of the alignment system during tests with the engineering detector unit (i.e. full-sized instrument chassis with a single detector in one of the compartments). To ease the identification of the components of the alignment system, the schematic drawing and the photo show the system from a similar perspective.

and vertically across the field of view. The X-ray source was a Varian VF-50 X-ray tube with Ti anode. The collimator consisted of 2 pinholes positioned 260.4 mm apart. Each pinhole had a diameter of 0.5 mm, and its vertical and horizontal position relative to the X-ray tube could be adjusted. The X-ray tube and the collimator were mounted on a common translation stage. The distance between the X-ray tube and the closest of the pinholes was 82.8 mm. The setup allows the insertion of an alignment laser between the X-ray tube and the collimator. The schematic view of the measurement setup is shown in the left panel of Fig. 9. The photo of the measurement setup is shown in the right panel of Fig. 9. The photo shows the engineering unit (i.e. a full-sized instrument chassis populated with only one detector) undergoing the test. The system arrangement for the flight instrument measurements was the same as the one presented in the photo, but with the engineering unit replaced with the flight instrument. The alignment procedure consisted of the following sequence of steps:

1. The pinhole closest to the X-ray tube was aligned with the center of the X-ray beam generated by the tube.

2. The collimator optical axis was aligned normal to a flat optical mirror glued to the instrument chassis between the DPU 14 and 54 detector units (see Fig. 1 and the left panel of Fig. 9). In this step, the laser was mounted behind the closest of the pinholes, the laser tilt and the position of the second pinhole were adjusted so that the laser beam reflected off the mirror passed through both pinholes. At this point the two pinholes defined a vector that was aligned with the normal to the mirror.

3. The center of each SDD Si chip was determined. The collimated X-ray beam was scanned across the aperture of each detector. The length of the collimator and the size of the pinholes used resulted in the X-ray beam of ~ 1.2 mm in diameter at the distance of the Si chip. The small size of the X-ray beam allowed to locate the center of the Si chip. The same analysis method as the one used to determine the size and the position of the FoV (see description below and Fig. 10) was used to determine the position of the SDD radiation-sensing chip.

4. The FoV was mapped. With the collimator removed (leaving a coarsely collimated and much brighter beam), the X-ray tube was used to scan across each aperture. Scans were used to determine the size and the position of the field of view of the individual detector units.

Figure 10 shows results of the FoV measurement for DPU 14. The left panel shows a count-

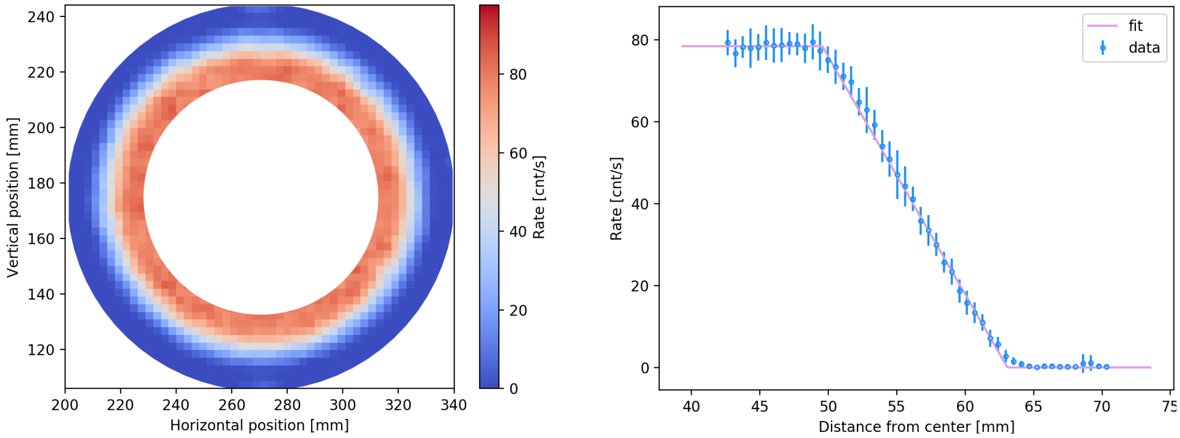

Fig 10 Left: Count-rate map obtained in the FoV scan. Color-coded is the count rate. X and Y values show horizontal and vertical positions of the X-ray source, respectively. Right: Projection of the count-rate map onto the rate-radius plane. The binned data are shown with blue points. A trapezoidal fit to the data is shown with violet solid line. To make the fit line clearly visible, the data had to be binned for plotting. Binning of the data reduced the number of points that needed to be plotted from $\sim$ 1100 to 50. The fit, however, was performed on the unbinned data set. Both plots show data obtained for DPU 14.

rate map while the right panel shows a projection of the count-rate map onto the rate-radius plane. Scanning only the region between full efficiency and zero response reduced the time necessary to execute Step 4 of the alignment procedure, and was warranted by the results of the FoV scan performed on the engineering unit. The dimensions of the FoV were determined from a trapezoidal fit to the projection of the (X, Y) count-rate map onto the rate-radius plane, where the radius is defined as a distance between the point where the rate was measured and the center of the FoV. The radius r was calculated with a simple formula $r = \sqrt{(X - X_0)^2 + (Y - Y_0)^2}$, where (X_0, Y_0) are the coordinates of the center of the FoV, and (X, Y) are the coordinates of the measurement point. The right plot in Fig. 10 shows the measured count rate as a function of the radius (points). The results of the trapezoidal fit are shown with a solid line. Two parameters fully describe the FoV of HaloSat detectors: the full- and the zero-response radius. The former is the radius at which the count rate stops being constant with radius, and starts linearly decreasing when moving away from the center of the FoV. The latter is the radius at which the count rate drops to zero. Table 6 shows

Table 6 Field of view parameters of the HaloSat detector units determined during the alignment scans.

DPU unit	Response radius (°) Full	Zero
14	4.998 ± 0.009	7.030 ± 0.003
38	5.028 ± 0.009	7.032 ± 0.003
54	5.016 ± 0.013	7.030 ± 0.001

the values of the full- and the zero-response radii measured for the HaloSat detector units. The determined FoV sizes are consistent between the units. The response-weighted effective field of view, averaged over the three units, is 0.035 steradians (or 115.02 deg^2).

The instrument grasp calculated using this response-weighted field of view and the effective area of 5.1 mm^2 around 600 eV is $\sim$ 17.7 cm^2 deg^2. This value is calculated assuming that all three detector units are operational. The achieved grasp value is close to the grasp goal (see Sec. 1 and Tab. 1). The requirement for the statistical accuracy of the oxygen line measurements (see Sec. 1) translates to a requirement on the combination of $EA \times FoV \times t_{obs}$, where t_{obs} is the observing time. To meet the statistical accuracy requirement, the instrument with a smaller grasp (e.g. in a hypothetical scenario where one of the HaloSat detector units fails) will need to increase its observing time.

The alignment procedure was also used to determine the bore-sight direction of the detector units and their relative co-alignment. Our measurements showed that the original set of the FoV washers provided good bore-sight co-alignment to within $0.20°$, and that there was no need for any additional adjustments to the detectors' FoV washers. The average of the three bore-sight vectors was used to relate the science instrument pointing to the spacecraft pointing as given by the spacecraft star-tracker system. Calibration of the co-alignment and bore-sight was repeated in orbit by scanning across the Crab Nebula and provides consistent results.[3]

5 Conclusions

The HaloSat science instrument underwent a series of TVAC tests to study its performance across a broad temperature range. Data obtained during those tests were used to create calibration products that include energy calibration, instrument energy resolution, and instrument response. In addition, the field of view and co-alignment were measured under lab conditions. The detectors are intrinsically quite similar, and we adopt a single response matrix suitable for all three detectors throughout the mission. The on-ground tests confirmed that the HaloSat science instrument meets the criteria necessary for the successful execution of its scientific objectives.

6 Acknowledgments

This research was supported by NASA grant NNX15AU57G and the Iowa Space Grant Consortium award NNX16AL88H. We would like to thank Tracy Behrens for her work in assembling the HaloSat electronics, Rich Dvorsky for his mechanical and polymerics advice, Brian Busch, Larry Detweiler, and Matt Miller for machining parts, Tim Cameron for building the HVPS, Kayla Racinowski for helping with polymerics and inductors, Jeff Dolan for his help with connectors and electronics, Jim Phillips for help with inductor cores, Drew Miles for early SDD testing, Keith White for mechanical design work, Jesse Haworth for the HVPS testing and designing the HaloSat logo, and Riley Wearmouth for early mechanical designs. We thank the Blue Canyon Technologies team for their work on the spacecraft bus and leading the mission operations. We are grateful to Thomas Johnson for being the project manager, Luis Santos for system engineering, John Hudeck for his assistance with vibration testing, and the Wallops Flight Facility Ground Station team for their support of the HaloSat in orbit. We also thank Systemyde International for supplying the Y90S, and Brian Mokrzycki for providing the Verliog for the FPGAs.

References

1 J. Puig-Suari, J. Schoos, C. Turner, *et al.*, *CubeSat developments at Cal Poly: the standard deployer and PolySat*, vol. 4136 of *Society of Photo-Optical Instrumentation Engineers (SPIE) Conference Series*, 72–78 (2000).

2 J. Puig-Suari, C. Turner, and W. Ahlgren, "Development of the standard cubesat deployer and a cubesat class picosatellite," *IEEE* **1**, 347–353 (2001).

3 P. Kaaret, A. Zajczyk, D. M. LaRocca, *et al.*, "HaloSat: A CubeSat to Study the Hot Galactic Halo," *ApJ* **884**(2), 162 (2019).

4 A. Zajczyk, P. Kaaret, D. Kirchner, *et al.*, "HaloSat: A Search for Missing Baryons with a CubeSat," in *Proceedings of the AIAA/USU Conference on Small Satellites*, *Upcoming Missions*, SSC18–WKIX–01. https://digitalcommons.usu.edu/smallsat/2018/all2018/471/.

5 D. M. LaRocca, P. Kaaret, A. Zajczyk, *et al.*, "Design and Construction of the X-ray Instrumentation On-Board the HaloSat Cube Satellite," *JATIS* **6**(1), 1 – 14 (2020).

6 https://www.amptek.com/products/sdd-x-ray-detectors-for-xrf-eds/fast-sdd-silicon-drift-detector

7 A. Thompson, D. Attwood, E. Gullikson, *et al.*, *X-Ray Data Booklet*, Lawrence Berkeley National Laboratory (2009).

8 G. W. Fraser, *X-ray Detectors in Astronomy* (1989).

9 G. F. Knoll, *Radiation detection and measurement* (2000).

10 F. Scholze and M. Procop, "Modelling the response function of energy dispersive X-ray spectrometers with silicon detectors," *X-ray Spectrometry* **38**, 312–321 (2009).

11 K. C. Gendreau, Z. Arzoumanian, P. W. Adkins, *et al.*, *The Neutron star Interior Composition Explorer (NICER): design and development*, vol. 9905 of *Society of Photo-Optical Instrumentation Engineers (SPIE) Conference Series*, 99051H (2016).

12 G. Prigozhin, K. Gendreau, J. P. Doty, *et al.*, *NICER instrument detector subsystem: description and performance*, vol. 9905 of *Society of Photo-Optical Instrumentation Engineers (SPIE) Conference Series*, 99051I (2016).

13 K. A. Arnaud, *XSPEC: The First Ten Years*, vol. 101 of *Astronomical Society of the Pacific Conference Series*, 17 (1996).

14 https://heasarc.gsfc.nasa.gov/docs/halosat/

Anna Zajczyk received her MSc in Astronomy from Nicolaus Copernicus University in 2007, and her PhD in Physics from the Polish Academy of Sciences' Nicolaus Copernicus Astronomical Center and Université Montpellier 2 in 2012. As the instrument scientist she led the calibration efforts for the HaloSat science instrument. Her current research interests focus on instrument development and instrument calibration for X-ray astronomy.

Philip Kaaret is Professor of Physics and Astronomy at the University of Iowa. He received his SB in Physics from the Massachusetts Institute of Technology in 1984 and his PhD in Physics from Princeton in 1989. He is the Principal Investigator of HaloSat.

Daniel LaRocca received his BA in Physics from Illinois Wesleyan University in 2013, and his PhD in Physics from the University of Iowa in 2020. He was a member of the team that built the HaloSat science payload and oversaw science operations scheduling for most of the mission.

List of Figures

List of Tables